

Low Thermal Conductivity Phase Change Memory Superlattices

Jing Ning^{1,2*}, Xilin Zhou³, Yunzheng Wang¹, Takashi Yagi⁴, Janne Kalikka⁵, Siew Lang Teo⁶, Zhitang Song³, Michel Bosman^{2,6} and Robert E. Simpson^{1*}

¹Singapore University of Technology and Design, 8 Somapah Road, 487372, Singapore.

²Department of Materials Science and Engineering, National University of Singapore, 9 Engineering Drive 1, 117575, Singapore.

³State Key Laboratory of Functional Materials for Informatics, Shanghai Institute of Microsystem and Information Technology, Chinese Academy of Sciences, 865 Changning Road, Shanghai, 200050, China.

⁴National Metrology Institute of Japan, National Institute of Advanced Industrial Science and Technology, Tsukuba Central 3, 1-1-1 Umezono, Tsukuba, Ibaraki, 305-8563, Japan.

⁵Computational Physics Laboratory, Tampere University, Tampere, FI-33014, Finland.

⁶Institute of Materials Research and Engineering (IMRE), Agency for Science Technology and Research (A*STAR), 2 Fusionopolis Way, 138634, Singapore.

*Corresponding author(s). E-mail(s):

jing_ning@mymail.sutd.edu.sg; robert_simpson@sutd.edu.sg;

Contributing authors: xilinzhou@mail.sim.ac.cn;

yunzheng_wang@sdu.edu.cn; t-yagi@aist.go.jp;

janne.kalikka@tuni.fi; sl-teo@imre.a-star.edu.sg;

ztsong@mail.sim.ac.cn; msemb@nus.edu.sg;

Abstract

Phase change memory devices are typically reset by melt-quenching a material to radically lower its electrical conductance. The high power

and concomitantly high current density required to reset phase change materials is the major issue that limits the access times of 3D phase change memory architectures. Phase change superlattices were developed to lower the reset energy by confining the phase transition to the interface between two different phase change materials. However, the high thermal conductivity of the superlattices means that heat is poorly confined within the phase change material, and most of the thermal energy is wasted to the surrounding materials. Here, we identified Ti as a useful dopant for substantially lowering the thermal conductivity of Sb_2Te_3 -GeTe superlattices whilst also stabilising the layered structure from unwanted disordering. We demonstrate via laser heating that lowering the thermal conductivity by doping the Sb_2Te_3 layers with Ti halves the switching energy compared to superlattices that only use interfacial phase change transitions and strain engineering. The thermally optimized superlattice has $(0\ 0\ 1)$ crystallographic orientation yet a thermal conductivity of just $0.25\ \text{W}\cdot\text{m}^{-1}\cdot\text{K}^{-1}$ in the "on" (set) state. Prototype phase change memory devices that incorporate this Ti-doped superlattice switch faster and at a substantially lower voltage than the undoped superlattice. During switching the Ti-doped Sb_2Te_3 layers remain stable within the superlattice and only the Ge atoms are active and undergo interfacial phase transitions. In conclusion, we show the potential of thermally optimised Sb_2Te_3 -GeTe superlattices for a new generation of energy-efficient electrical and optical phase change memory.

Keywords: Phase Change Memory, Thermal Conductivity, Strain engineering

1 Introduction

Data is being created, stored, and processed at a staggering rate. Indeed, the world's data production doubles in size every two years and by 2025 it is predicted to reach a whopping 181 zettabytes per year [1], whilst the data storage demand is predicted to be 30.23 zettabytes in 2030 [2]. This exponential growth in data production and storage is fueling innovations in materials, device scaling, and novel data storage concepts. Consequently, the amount of energy consumed to store the world's data is expected to have a 17% reduction from 18.33 TWh in 2016 to 15.23 TWh in 2030 [2].

High speed and low energy prototype resistive [3], ferroelectric [4], magnetoelectric [5], and phase change [6] memories are all currently being developed. Phase change memories are currently leading the way and are being produced commercially. Phase change memory encodes data in the local structural order of a phase change material (PCM), and the data is read as a substantial electrical resistance change, which results from the different structural states. Typically, the amorphous and crystalline states of the PCM are used to encode binary information into the material. The amorphous to crystalline (SET) transition is induced by heating the material for a duration sufficiently long that the atoms can overcome an energy barrier and move into a lower energy configuration. The reversible transition from the crystalline (SET) phase to the amorphous (RESET) phase is realized by melt-quenching the material at a rate higher than the crystallization rate, such that the atoms are frozen in a higher energy state. Many chalcogenide materials, especially those along the Sb_2Te_3 – GeTe pseudo-binary tie-line in the Ge–Sb–Te ternary diagram exhibit rapid recrystallization that results in a substantial electrical and optical contrast. Arguably, $\text{Ge}_2\text{Sb}_2\text{Te}_5$ is the most famous of these materials. $\text{Ge}_2\text{Sb}_2\text{Te}_5$ -based compounds have been widely studied and commercially applied in DVD-RAM optical discs [7] and the 3D X'point technology electrical memory [8].

Despite their commercial success, the main drawback with PCM-based electrical data storage is the high RESET power. Generally, the PCM RESET current needs to be lower than the ON-state current of the memory cell selector. To achieve high data densities, two terminal ovonic threshold selectors (OTS) are replacing their three terminal transistor counterparts [9]. However, the current density of an OTS tends to be lower than transistor selectors, and most selectors can only pass a current up to ~ 10 MA/cm² [10]. Therefore, the RESET current density of the PCM must be limited below the ON-state OTS current, which is a big problem because longer pulse times are required to reset the PCM as a compromise, and this increases the phase change memory access time. We note, however, that most of the heat generated during the RESET process is dissipated into the surroundings and only 1% of the energy is actually used to drive the PCM phase transitions [11]. By decreasing the heat dissipated from the PCM element, there is a clear opportunity to decrease the RESET current and concomitantly decrease the PCM device access time.

Substantial research has focused on decreasing the energy consumed to switch PCMs, and three approaches have emerged to improve the switching efficiency: (1) Decrease the thermal conductivity; A variety of dopants to lower the switching current have been investigated, such as C [12], Cr [13], Sc [14], and Ti [15]. These dopant atoms diffuse into the PCMs to form local defects or distortions, which results in low thermal conductivity. The generated heat is confined in the PCM, which in turn leads to low energy switching. Similarly, a "superlattice-like" structure, which consists of non-epitaxial Sb_2Te_3 and GeTe stacked layers, was proposed to lower the switching energy by decreasing the thermal conductivity via interfacial phonon scattering [16]. More recently, several reports have demonstrated how two-dimensional crystals, such as graphene, MoS_2 , and WS_2 can be placed at the interface between the PCM and the electrode or substrate to confine heat through increased thermal boundary resistance [17–19]. (2) Decrease entropic losses; Interfacial phase change materials (iPCMs) improve the switching performance by limiting the movement of the atoms during the phase transition. Less movement freedom reduces entropic losses [20] and concomitantly decreases the energy required to switch the material. The iPCM structure, which also has a Sb_2Te_3 –GeTe layered structure but with a high degree of crystallographic orientation and lattice matching, was reported to have a higher thermal conductivity than both the $\text{Ge}_2\text{Sb}_2\text{Te}_5$ and the superlattice-like structure. Recently, however, the cross-plane thermal conductivity of the Sb_2Te_3 –GeTe superlattices was shown to decrease with increasing number of Sb_2Te_3 –GeTe interfaces [21]. We conclude, therefore, that both thermal confinement effects and smaller entropic losses contribute to the lower switching energy seen in iPCM devices. (3) Decrease the activation energy for the Ge atomic transitions; that the activation energy for atomic transitions in the iPCM structure can be controlled using strain engineering; indeed, straining the GeTe layer by just 2.1% leads to substantial decrease in the switching voltage. The Ge atom interfacial transition is an activated process. Biaxially straining the superlattice makes the Ge atom transition easier, thus lowering the switching energy of iPCM devices [22, 23]. All these methods can improve the switching performance to some extent, however, until now they have not been combined into a thermally-engineered, strain-engineered, interface-engineered "Super iPCM".

In this work, a highly efficient $[\text{Ti-Sb}_2\text{Te}_3]_{4\text{nm}}-[\text{GeTe}]_{1\text{nm}}$ iPCM superlattice structure, which exhibits interfacial atomic transitions, strain-engineered layers, and low thermal conductivity is designed and demonstrated in a prototype memory cell. Adding Ti into bulk Sb_2Te_3 primarily increases phonon scattering from point defects and consequently decreases the thermal conductivity [24]. If this same effect exists in Sb_2Te_3 textured thin films, then one should expect a substantial decrease in the iPCM thermal conductivity. This decrease should be especially dramatic in the strain engineered iPCM structure where the Sb_2Te_3 layers are four times thicker than the GeTe layers. It is therefore hypothesized that doping Ti into Sb sites in the Sb_2Te_3 crystal will be an effective way to lower the thermal conductivity of the whole superlattice

structure. Clearly, the Ti atoms must not interfere with the Ge atomic interfacial transitions, nor with the strain in the GeTe layers for the structure to maintain lower entropic losses and lower activation energy.

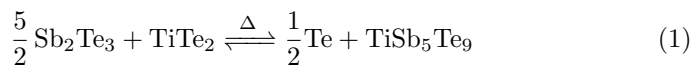
Herein, we show radically lower switching energies are possible by doping the Sb₂Te₃ layers with Ti. The Ti-doped Sb₂Te₃ superlattice structure can retain a highly out-of-plane crystallographic orientation for Ti concentrations up to 3.6 at.%. The thermal conductivity of the Sb₂Te₃–GeTe layers is lowered by over 50% when 3.6 at.% Ti is doped into the structure. Density Functional Molecular Dynamics (DF/MD) simulations confirm that the GeTe layers disorder at a lower temperature than the Ti-Sb₂Te₃ layers, which is a fingerprint of the interfacial switching and demonstrates the stability of the Ti-Sb₂Te₃ layers [22]. Subsequently, we study the switching performance of this super iPCM using laser pulses. The Ti-doped iPCM superlattice structure RESET switching energy is halved, and the pulse widths of 10 ns are enough to switch the material. When this Ti-doped iPCM is incorporated into prototype memory cells, we show that the programming voltage is reduced by 30%. Moreover, the iPCM device for multilevel data storage application is demonstrated showing well separated four resistance states by doping TiTe₂ into the Sb₂Te₃ scaffold material of the iPCM. These results show that carefully designing the iPCM thermal properties is a viable method to meet the switching speed and energy requirements of future high speed phase change memory architectures, such as those using OTS selectors.

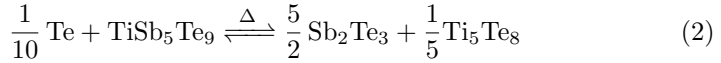
2 Results and Discussion

2.1 Highly (0 0 l) orientation

The efficient switching in iPCM relies on the interfaces between the Sb₂Te₃ and GeTe blocks being terminated with Te, which enables van der Waals (vdW) bonding between the blocks, as shown in Fig. 1(a). It is, therefore, critical to ensure that this feature of the superlattice structure is maintained when any dopants are added to one of the layers.

A series of Ti-doped Sb₂Te₃ were grown to study how the Ti dopant concentration influences the vdW layered structure. Low-power RF-co-sputtering from TiTe₂ and Sb₂Te₃ targets was used to grow a series of Ti_x–(Sb₂Te₃)_{1–x} films at 300 °C. These Ti_x–(Sb₂Te₃)_{1–x} films maintained a highly (0 0 l) oriented structure for all doping concentrations studied. However, Ti-doped Sb₂Te₃ without phase separation was only possible within a narrow doping Ti concentration window, as shown by their XRD patterns in supplementary Fig. S1(a). This is due to there being the following two chemical equilibria in Sb₂Te₃ and TiTe₂ co-sputtering:





At relatively low Ti concentrations, free energy and formation energy analysis reveals that the TiTe_2 enters vdW gap and then Ti atoms substitute Sb atoms to form TiSb_5Te_9 , see supplementary Fig. S2. This Ti substitution for Sb picture is consistent with the experimentally observed decrease in hole concentration due to Ti doping Sb_2Te_3 single crystals [24]. Crystal Orbital Hamiltonian Population (COHP) analysis reveals that this Ti for Sb substitution increases the stability of the superlattice, see supplementary Fig. S3. Again, an observation that is consistent with Ti dopants releasing an electrons into the conduction band that can recombine with holes [24] to decrease the overall energy of the system and increase the stability. As the concentration of TiTe_2 increases, as per Reaction 1, the structure phase separates into TiSb_5Te_9 , and free Te. Conveniently, however, Te has a low sticking coefficient at elevated temperatures and this facilitates the synthesis of TiSb_5Te_9 textured films, as per Reaction 2. Naturally, diffraction peaks associated with the Te or Ti_5Te_8 are seen when TiTe_2 is sputtered at the highest rates because separated Te or Ti_5Te_8 phase exists in the film. The texture of $\text{Ti}_x\text{-(Sb}_2\text{Te}_3)_{1-x}$ retains a layered (0 0 *l*) preferred orientation for $1.7 \leq x \leq 3.6$ at.% Ti, and peaks associated with phase separation into TiTe_2 , Te and Ti_5Te_8 are not present in the XRD patterns. In section 2.2, we see that $x = 3.6$ at.% Ti has the lowest thermal conductivity. This is important because it shows that low thermal conductivity vdW layered structures are possible without phase separation.

We grew high quality $\text{Ti}_{3.6}\text{-(Sb}_2\text{Te}_3)_{96.4}\text{-GeTe}$ superlattice, which were hypothesized to have a lower thermal conductivity than its undoped $\text{Sb}_2\text{Te}_3\text{-GeTe}$ counterpart. The hexagonal crystal structure has (0 0 *l*) texture with alternating layers of $\text{Ti}_{3.6}\text{-(Sb}_2\text{Te}_3)_{96.4}$ and GeTe stacked along the [1 1 1] direction of their rhombohedral primitive cells. Compared with the XRD patterns of the Ti- Sb_2Te_3 layers, the superlattice has two extra diffraction peaks at 25.1° and 51.5° that correspond to the (0 0 *l*) reflections of hexagonal GeTe. Both doped and undoped superlattice films retained a high (0 0 *l*) crystallographic orientation, as shown in Fig. 1(b). The slightly lower intensity and broader diffraction peaks in the Ti-doped superlattice structure is due to a smaller in-plane grain size and local distortions induced by Ti dopants. The XRD patterns clearly show that the Ti-doped superlattice film still retains the preferred out-of-plane orientation.

To confirm the influence of Ti on the local crystal structure, Raman spectra were measured with and without the Ti dopant. The spectra are shown in Fig. 1(c). Here, we highlight the Sb_2Te_3 and GeTe phonon modes in black and red dot-and-dash lines respectively. A_{1g}^1 (69 cm^{-1}), E_g^2 (109 cm^{-1}), and E_{1g}^2 (167 cm^{-1}) modes seen in the Sb_2Te_3 film have been reported before [23]. The Ti-doped Sb_2Te_3 layers retain the characteristic peaks of Sb_2Te_3 with a weak shoulder at 120 cm^{-1} . This signal is from in-plane vibrations of Ti-Te or Te-Te bonds. Hence, we conclude that the Ti atoms successfully substitute Sb atoms within the Sb_2Te_3 quintuple blocks. Note, the evolution of the Sb_2Te_3 vibrational modes with Ti concentration is shown in supplementary

Fig. S1(b). New modes between 120 cm^{-1} and 130 cm^{-1} emerge in the Sb_2Te_3 Raman spectra when TiTe_2 is co-sputtered with Sb_2Te_3 . The corresponding XRD patterns in supplementary Fig. S1(a) exhibit a similar diffraction peak that appears and disappears according to phase separation into TiTe_2 , Te , and Ti_5Te_8 as the concentration of TiTe_2 increases. The characteristic peaks associated with layered Sb_2Te_3 are well-preserved when the Ti concentration is in the range of 1.7–3.6 at.% and phase separation does not occur in this doping range.

Importantly, the Raman spectra also indicate that Ti helps to prevent intermixing of the superlattice layers. Comparing the $\text{Ti}_{3.6}\text{-(Sb}_2\text{Te}_3)_{96.4}\text{-GeTe}$ and the undoped $\text{Sb}_2\text{Te}_3\text{-GeTe}$ superlattice structures, we see that the E-mode at 79 cm^{-1} from GeTe is clearly visible in the $\text{Ti}_{3.6}\text{-(Sb}_2\text{Te}_3)_{96.4}\text{-GeTe}$ superlattice structure and less prominent in the undoped structure. The E-mode for GeTe is an in-plane vibration and its presence indicates that its in-plane structure has not been disturbed. Preventing intermixing is important since the low energy switching in iPCM is based on confining the Ge-atoms movement at the interfaces rather than diffusing through the whole structure. Thus, the loss of the layered structure increases the RESET switching current of PCM devices [20, 25, 26].

The layered structure of the $\text{Ti}_{3.6}\text{-(Sb}_2\text{Te}_3)_{96.4}\text{-GeTe}$ superlattice is also shown in the cross-sectional STEM image. The superlattice layers clearly form blocks that are separated by vdW gaps, as shown in Fig. 1(d). The corresponding FFT image shows a series of streaks consisting of more closely spaced spots. This is a typical pattern for a large crystal unit cell exhibiting periodic superlattice layers in real space. The electron diffraction FFT analysis reveals out-of-plane layering with a period of $46.37 \pm 0.20\text{ \AA}$, which agrees well with the simulated c-axis of the corresponding unit cell (46.65 \AA), as seen in Fig 1(a). We conclude that the fabricated $\text{Ti}_{3.6}\text{-(Sb}_2\text{Te}_3)_{96.4}\text{-GeTe}$ superlattice structure exhibits (0 0 *l*) layering and is similar to the model presented in Fig 1(a), which we used for our DFT calculations.

We have shown unequivocally using XRD, Raman spectroscopy, and STEM imaging that the $\text{Ti}_{3.6}\text{-(Sb}_2\text{Te}_3)_{96.4}\text{-GeTe}$ superlattice exhibits a high quality layered structure. The fact that Ti dopants can be introduced into the superlattice quintuple Sb_2Te_3 layer opens new possibilities for tuning the superlattice properties. In the subsequent section, we will show how the thermal conductivity of the superlattice is substantially lower than its undoped counterpart.

2.2 Lowering the thermal conductivity

PCMs with a low thermal conductivity improve the switching energy efficiency by confining the generated Joule heat within the PCM rather than allowing the heat to diffuse into the surrounding materials. Therefore, we deliberately doped the Sb_2Te_3 layers of the superlattice structure with Ti to improve its switching energy performance. Ti was chosen because it was found to decrease

the thermal conductivity of Sb_2Te_3 bulk single crystals. Herein, we report time-dependent thermal reflectance (TDTR) measurements that show how Ti has a dramatic effect on the thermal conductivity of $(0\ 0\ l)$ textured Sb_2Te_3 thin films. The thermal conductivity of Sb_2Te_3 exhibits a parabolic dependence on the Ti concentration, as shown in Fig. 2(a). The measured thermal conductivity of Sb_2Te_3 was $\sim 0.64\ \text{W}\cdot\text{m}^{-1}\cdot\text{K}^{-1}$, which is consistent with previously reported values in the literature [27–29]. The lowest thermal conductivity was observed for Ti concentrations between 3.6 at% and 6 at%. In section 2.1, we found that for Ti concentrations greater than 3.6 at% resulted in phase separation. Therefore, the 3.6 at% Ti-doped sample exhibits both a textured structure and low thermal conductivity, which when incorporated into a superlattice structure should allow both interfacial atomic transitions and efficient heat trapping.

The effect of Ti on the superlattice thermal conductivity was confirmed by comparing the thermal conductivity of undoped Sb_2Te_3 –GeTe and $\text{Ti}_{3.6}$ – $(\text{Sb}_2\text{Te}_3)_{96.4}$ –GeTe superlattice structures. The thermal conductivity of the undoped Sb_2Te_3 –GeTe superlattice structure was measured to be $0.49\ \text{W}\cdot\text{m}^{-1}\cdot\text{K}^{-1}$ in the set (on) state whilst the $\text{Ti}_{3.6}$ – $(\text{Sb}_2\text{Te}_3)_{96.4}$ –GeTe superlattice thermal conductivity was more than halved, to just $0.24\ \text{W}\cdot\text{m}^{-1}\cdot\text{K}^{-1}$, as shown in Fig. 2(a). The decreasing thermal conductivity is generated from the Ti-induced point defects and local distortions within its crystalline grains (see Fig. 1(d)) [15, 24]. These results suggest that the Ti doped superlattice should switch substantially more efficiently than its undoped counterpart.

The topography of the Ti-doped superlattice film suggests the presence of much smaller crystal grain sizes than that for the undoped superlattice. The mean grain diameter of the doped superlattice structure is ~ 20 – $40\ \text{nm}$ whilst it is ~ 80 – $110\ \text{nm}$ in the undoped superlattice, as shown in Fig. 2(b) and (c). Similar features are observed in the SEM images, which are included in the supplementary section for the interested reader, see Fig. S4. The smaller grains improve the film uniformity and result in smoother films. Indeed, the AFM-measured RMS roughness decreased from $3.62\ \text{nm}$ for the undoped structure to $1.47\ \text{nm}$ for the doped structure. Smoother films are preferred when building multilayered 3D device architectures because the effect of layer roughness needs to be minimized.

2.3 Low Switching Energy Ti-doped superlattices

An important design consideration for iPCM superlattice structures is an active layer that switches and is embedded in a stable scaffold [22]. Indeed, the GeTe layers embedded within the Sb_2Te_3 or Sb_2Te_1 scaffold exhibit premelting, which is similar to amorphization but limited to the GeTe layers. The Sb_2Te_3 films remain crystalline and the layered structure is uncompromised [22, 30]. It is, therefore, important to confirm whether the $\text{Ti}_{3.6}$ – $(\text{Sb}_2\text{Te}_3)_{96.4}$ –GeTe superlattice also exhibits premelting.

The melting behavior of the $\text{Ti}_{3.6}\text{-(Sb}_2\text{Te}_3)_{96.4}\text{-GeTe}$ superlattice was studied using DF/MD simulations from 450 K to 1200 K in 375 ps, as shown in Fig. 3. The crystallinity of the individual GeTe and Ti-Sb₂Te₃ layers was calculated as a function of temperature and time using the Steinhardt bond-orientation parameter [31]. The initial structure was fully ordered and the crystallinity was equal to 1, whilst it fully disorders when the temperature exceeds 1135 K, as shown in the inset of Fig. 3. We also see that the GeTe layer disorders at a much lower temperature than the $\text{Ti}_{3.6}\text{-(Sb}_2\text{Te}_3)_{96.4}$ layer; i.e. the superlattice does indeed exhibit GeTe premelting. The GeTe starts disordering at 650 K, whilst the $\text{Ti}_{3.6}\text{-(Sb}_2\text{Te}_3)_{96.4}$ scaffold layers remain highly ordered up to ~ 850 K. The crystallinity of GeTe is reduced by 20% to 0.8 at 1025 K whilst the $\text{Ti}_{3.6}\text{-(Sb}_2\text{Te}_3)_{96.4}$ layer cannot reach this level until the whole structure completely melted. This result provides strong evidence that Ti-doped Sb₂Te₃ can efficiently switch by premelting the GeTe layers within the superlattice. Importantly, the $\text{Ti}_{3.6}\text{-(Sb}_2\text{Te}_3)_{96.4}\text{-GeTe}$ superlattice exhibits a substantially lower thermal conductivity than the undoped superlattice yet it maintains the GeTe premelting characteristic, both of which will enable low-energy switching.

A PCM that can switch at high speed with low energy pulses is important for short access times in memory devices. We used a pump-probe laser system to measure the switching energy and time of the doped and undoped superlattices [32]. The as-grown crystalline Ti-doped Sb₂Te₃-GeTe superlattice films were irradiated with laser pulses with different durations and powers. The optical reflectivity of the film decreased as the laser energy deposited into the film increased. This is indicating a phase transition between the two structural phases. The laser pulse power-time-reflectivity for the Sb₂Te₃-GeTe and $\text{Ti}_{3.6}\text{-(Sb}_2\text{Te}_3)_{96.4}\text{-GeTe}$ superlattices are presented in Fig. 4(a) and (b) respectively.

The reset switching energy of the $\text{Ti}_{3.6}\text{-(Sb}_2\text{Te}_3)_{96.4}\text{-GeTe}$ superlattice is nearly three times lower than that of the undoped Sb₂Te₃-GeTe superlattice. The laser power-time-reflectivity curves, which are shown in Fig. 4, reveal that the undoped superlattice required ~ 28.72 mW, 60 ns (1.72 μJ) RESET pulses. In contrast, the $\text{Ti}_{3.6}\text{-(Sb}_2\text{Te}_3)_{96.4}\text{-GeTe}$ superlattice was reset with just ~ 13.45 mW and 50 ns (0.67 μJ) pulses; which corresponds to a $2.6\times$ reduction in switching energy. The only difference between the two superlattices is their thermal conductivity due to Ti doping the low switching energy structure. Fig. 2 shows that the thermal conductivity of the $\text{Ti}_{3.6}\text{-(Sb}_2\text{Te}_3)_{96.4}\text{-GeTe}$ superlattice is approximately half that of the undoped superlattice.

To a first approximation, the characteristic time for heat conduction through a material is $\Delta t \approx \frac{x^2 \rho C_p}{\kappa}$, where x is the distance from the laser heat source to the substrate, κ is the thermal conductivity, ρ is the density and C_p is the heat capacity. Thus, the distance over which heat diffuses depends on the square root of the thermal conductivity. Here, the thermal conductivity of the doped superlattice is half that of the undoped superlattice. Therefore, the $\text{Ti}_{3.6}\text{-(Sb}_2\text{Te}_3)_{96.4}\text{-GeTe}$ superlattice confines the heat within a diameter that

is approximately 1.4 smaller than that of the undoped superlattice. Since heating is governed by an imbalance in the heat flux in and out of the film, reducing the rate that heat can diffuse out of the structure leads to heat confinement and enables the GeTe layers to premelt-disorder with lower input energies.

The $\text{Ti}_{3.6}\text{-(Sb}_2\text{Te}_3)_{96.4}\text{-GeTe}$ superlattice layered structure is stable even after laser resetting. The superlattice is remarkably stable and even after resetting at the ~ 33.42 mW power limit of our laser, subsequent cross-sectional TEM analysis shows a layered structure, see Fig. 4(c). The streaks and additional spots in the TEM selected area electron diffraction pattern (inset) also show that the superlattice structure remains layered and is similar to the as-grown superlattice. The uncapped structure could be cycled between the SET and RESET states more than 4000 times using 13.45 mW for 50 ns RESET pulses and 9.42 mW for 300 ns SET pulses. These results are provided in Fig S5 of the supplementary section. We expect higher cycle abilities in electrical memory devices because the structure is protected from the atmosphere by the surrounding materials.

The $\text{Ti}_{3.6}\text{-(Sb}_2\text{Te}_3)_{96.4}\text{-GeTe}$ superlattice is heated more rapidly and reaches a substantially higher equilibrium temperature than the undoped $\text{Sb}_2\text{Te}_3\text{-GeTe}$ superlattice when irradiated with the same laser pulse parameter. The minimum laser powers needed to RESET the superlattices with 70 ns pulses were found from the power-time-reflectivity matrices, see Fig. 4(a) and (b). They were respectively 28.72 mW and 13.45 mW for the $\text{Sb}_2\text{Te}_3\text{-GeTe}$ and $\text{Ti}_{3.6}\text{-(Sb}_2\text{Te}_3)_{96.4}\text{-GeTe}$ superlattices. The finite-difference method was then used to simulate the cross-sectional temperature distribution in the superlattices as a function of time during these RESET pulses. Both superlattice samples reached a similar temperature (over 900 K) after 70 ns, as shown in Fig. S6, which is sufficient for premelt disordering, hence we observe a transition to the RESET reflectivity state in Fig. 4(a) and (b). Importantly, however, the laser power used to RESET the $\text{Ti}_{3.6}\text{-(Sb}_2\text{Te}_3)_{96.4}\text{-GeTe}$ superlattice was only 47% of that needed to RESET the undoped structure; a substantial switching energy efficiency improvement. To emphasize the difference in heating efficiency, the temperature rise in the two structures due to irradiating with the same 70 ns for 13.45 mW laser pulses was simulated. The equilibrium temperature difference between the two superlattices was 321 K, as shown in Fig. 4(d). The temperature distributions at 70 ns are also inset into Fig. 4(d). The undoped superlattice temperature does not even reach 600 K and remains well below the GeTe premelt disordering temperature. Therefore, the undoped superlattice cannot RESET with 70 ns 13.45 mW pulses. These simulations highlight the substantial difference in heating efficiency and agree well with our laser switching experiments.

The substantial improvement in heating efficiency implies a reduction in the switching voltage when these superlattices are employed in electrical phase change memory cells. The reversible resistance-voltage (R-V) switching measurement for the undoped $\text{Sb}_2\text{Te}_3\text{-GeTe}$ and $\text{Ti}_{3.6}\text{-(Sb}_2\text{Te}_3)_{96.4}\text{-GeTe}$ superlattices devices is given in Fig. 4(e) and (f). The pulse duration on

the R-V switching curves was 20 ns and 40 ns. The $\text{Ti}_{3.6}\text{-(Sb}_2\text{Te}_3)_{96.4}\text{-GeTe}$ superlattices device showed over two orders of magnitude change in electrical resistance between the SET and RESET states, which is larger than that of undoped superlattice device. The Ti-doped iPCM cell started to switch with 20 ns pulses and two orders of magnitude change was possible when the pulse time was 40 ns. With 40 ns pulses, the undoped superlattice (1.6 ± 0.1 V) and $\text{Ti}_{3.6}\text{-(Sb}_2\text{Te}_3)_{96.4}\text{-GeTe}$ superlattice can be set with a similar programming voltage of 1.65 ± 0.15 V. The thermal effect has an even greater influence on the RESET voltage because of the higher temperature needed for premelt-disordering. The undoped superlattice resets at 3.4 ± 0.1 V whereas the $\text{Ti}_{3.6}\text{-(Sb}_2\text{Te}_3)_{96.4}\text{-GeTe}$ structure resets at 2.65 ± 0.25 V with 40 ns pulses. The less abrupt switching occurred in $\text{Ti}_{3.6}\text{-(Sb}_2\text{Te}_3)_{96.4}\text{-GeTe}$ superlattices device, showing the possibility for multi-level operation. In the supplementary section, we have also included the DC current-voltage (I-V) curves, see Fig. S7. The superlattices exhibit ovonic threshold switching [33] whereby the disordered GeTe layers in the RESET state produce a voltage snapback and increase in conductivity at a threshold voltage V_{th} . The V_{th} of the $\text{Ti}_{3.6}\text{-(Sb}_2\text{Te}_3)_{96.4}\text{-GeTe}$ superlattice devices was lower than that of the undoped devices. This lower OTS voltage is indicative of a structure with more charged defects, which is consistent with Ti atoms substituting Sb atoms to producing positively charged defects [24]. All of these electrical switching results show that Ti improves the heating efficiency of the superlattice without negatively affecting the electrical resistance change.

3 Conclusion

We have shown that the switching energy of interfacial phase change memory superlattices can be further improved by doping the Sb_2Te_3 layers with elements that lower their thermal conductivity. Indeed, when the thermal conductivity of the superlattice is halved, the RESET switching energy also decreases by 50%. As with the undoped superlattice, the GeTe layers in the Ti-doped superlattice premelt-disorder before the superlattice completely amorphizes. Indeed, the layered structure is robust and present even after switching into the high resistance state.

Thermal conductivity is an important knob that can be used to enhance the iPCM switching energy efficiency. Titanium is just one dopant that we have identified that can lower the superlattice thermal conductivity without influencing the crystal structure and the interfacial switching mechanism. We suspect that other elements can also provide similar benefits. Generally, this work highlights the importance of co-optimizing the crystal structure, thermal conductivity, entropy, and strain to achieve a low energy switching phase change material. We expect that these super-iPCM materials will be applied in the next generation of high speed, energy efficient nonvolatile memory technologies.

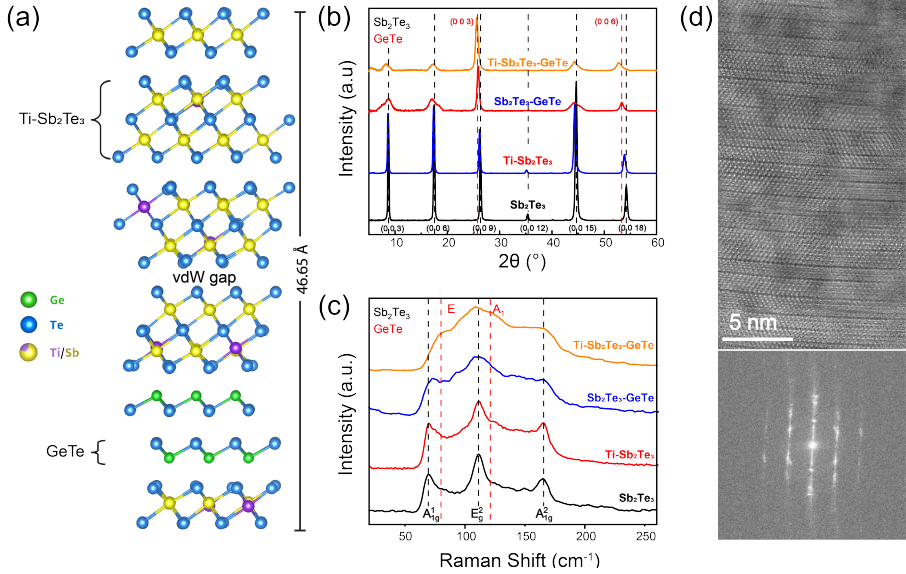


Fig. 1 Structure of the Ti-doped superlattice. (a) Schematic of the $[\text{Ti-Sb}_2\text{Te}_3]_{4nm}-[\text{GeTe}]_{1nm}$ superlattice crystal structure. (b) XRD patterns of pure Sb_2Te_3 and Ti-doped Sb_2Te_3 and their superlattice films. (c) Raman spectra of pure Sb_2Te_3 and Ti-doped Sb_2Te_3 and their superlattice films. (d) Cross-section TEM image of $[\text{Ti-Sb}_2\text{Te}_3]-[\text{GeTe}]$ superlattice layers and the corresponding FFT image of this area.

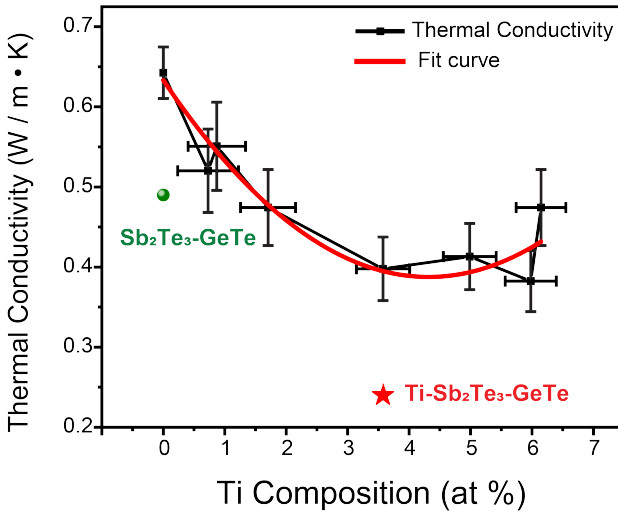
4 Methods

4.1 Superlattice growth and memory device fabrication

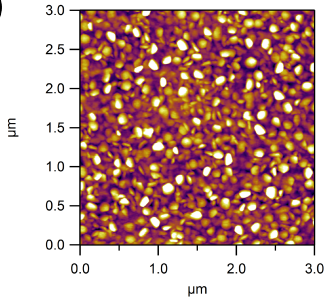
The series of Ti-doped Sb_2Te_3 and $\text{Ti}_{3.6}-(\text{Sb}_2\text{Te}_3)_{96.4}-\text{GeTe}$ superlattice films were deposited on Si (1 0 0) substrate by magnetron sputtering. The background pressure of the main chamber was kept better than 6×10^{-5} Pa and the samples were prepared with an Ar atmosphere at a pressure of 0.5 Pa. The native silicon oxide layer on the Si substrate was removed by plasma etching at 25 W in an Ar atmosphere of 0.5 Pa for 60 min prior to the deposition. A 4-nm-thick amorphous Sb_2Te_3 was deposited at room temperature as seed layer and the further thin films were grown at 300°C [34, 35]. The films were cooled to room temperature in the vacuum chamber to avoid oxidation. The Ti-doped Sb_2Te_3 layers were grown by co-sputtering from Sb_2Te_3 and TiTe_2 alloy targets (2" diameter and 99.999% pure from AJA International).

The phase change random access memory devices were formed by alternately stacking 4-nm-thick $\text{Ti-Sb}_2\text{Te}_3$ and 1-nm-thick GeTe layers on a mushroom-type device die. This PCM device die was fabricated using standard CMOS processing. The W bottom electrode was ~ 210 nm in diameter. The Ti-doped $\text{Sb}_2\text{Te}_3-\text{GeTe}$ superlattices were integrated into these prototype PCM devices by alternately stacking 4-nm-thick $\text{Ti-Sb}_2\text{Te}_3$ and 1-nm-thick GeTe layers. The total of 6 layer repeats were used to make a 30 nm thick

(a)



(b)



(c)

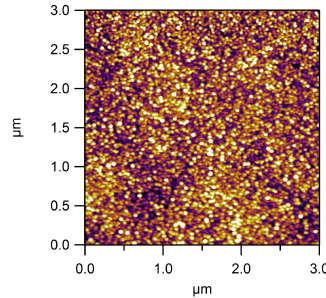


Fig. 2 (a) Thermal conductivity of Ti-doped Sb_2Te_3 films and superlattices. AFM topography of (b) undoped $\text{Sb}_2\text{Te}_3\text{-GeTe}$ and (c) Ti-doped $\text{Sb}_2\text{Te}_3\text{-GeTe}$ superlattice.

superlattice film. Including the 4 nm seed layer, the total PCM thickness was 34 nm. A 20 nm thick TiN top electrode contact (TEC) was sputtered from a Ti sputtering target in a reactive Ar:N₂ atmosphere at a pressure of 0.5 Pa. Finally, a 300 nm thick Al film was deposited on the TiN TEC to form a good electrical contact with the probing station. The $\text{Ti}_{3.6}\text{-(Sb}_2\text{Te}_3)_{96.4}\text{-GeTe}$ superlattice phase change memory device was benchmarked against an undoped $\text{Sb}_2\text{Te}_3\text{-GeTe}$ superlattice. It was also grown on a 4 nm thick Sb_2Te_3 seed layer and was formed by alternately stacking 4 nm Sb_2Te_3 and 1 nm GeTe layers using 6 repeats. With the exception of the Ti dopant, the devices were identical.

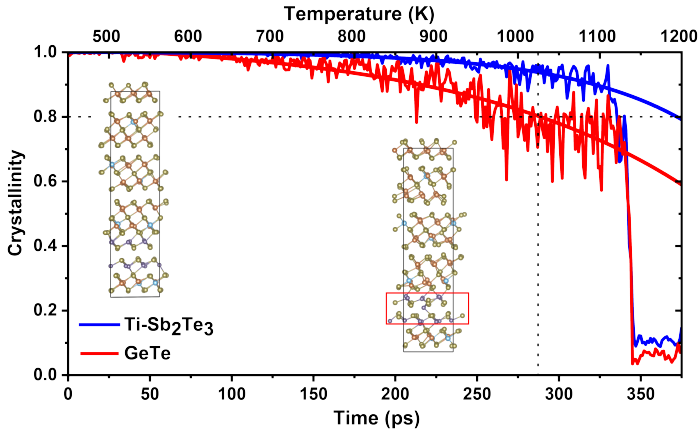


Fig. 3 Simulated premelting behavior of Ti-doped Sb_2Te_3 -GeTe from 450 K to 1200 K. The inset shows the crystal structure at 450 K and 1135 K respectively.

4.2 Characterization

The crystal quality and orientation of films were measured by X-ray diffraction (XRD, Bruker D8 Discover) with $\text{Cu K}\alpha$ ($\lambda=1.5418 \text{ \AA}$) radiation in a symmetric Bragg-Brentano geometry for θ - 2θ ranging from 5° to 60° . The morphology and topography of the films were analyzed by field-emission scanning electron microscopy (SEM, JEOL-7600F) and atomic force microscopy (AFM, Asylum Research, MFP-3D). The composition of the Ti-doped Sb_2Te_3 films was measured using energy dispersive spectroscopy (EDS) in the SEM. Raman spectra were obtained at room temperature by confocal Raman microscopy (WITec Alpha300R) with a 532 nm laser as the excitation source. Thermal conductivities of the films were obtained by time-domain thermoreflectance (TDTR) [36, 37]. The TDTR apparatus was equipped with an electrical delay control system, in which pulse emissions of two lasers were synchronized to an arbitrary function generator with 50 ns of delay range. The wavelength, repetition rate, pulse duration, average power, and spot radius of the pump laser were 1550 nm, 20 MHz, 0.5 ps, 20 mW, and $35 \mu\text{m}$, respectively. For the probe laser, the wavelength, average power and spot radius were 775 nm, 1 mW, and $15 \mu\text{m}$, respectively. The intensity of the pump laser was modulated by a rectangular wave of 200 kHz for lock-in detection. A 90-nm Al film was deposited on the top of samples as a transducer layer. The thermal conductivities of all samples were determined by fitting the measured thermoreflectance phase signals with those calculated from the delay time in the range from 0.2 to 50 ns. The sample structure was measured using scanning transmission electron microscopy (S/TEM, JEOL/FEI Titan) with an acceleration voltage of 200 kV, as shown in Fig. 1(d) and 4(c). Focused Ion Beam (FIB, FEI Helios Nanolab 450S) milling was necessary to prepare the lamella for cross-sectional TEM image. The optical switching was carried out using our home-made static tester, which consists of a high-power 658 nm pump

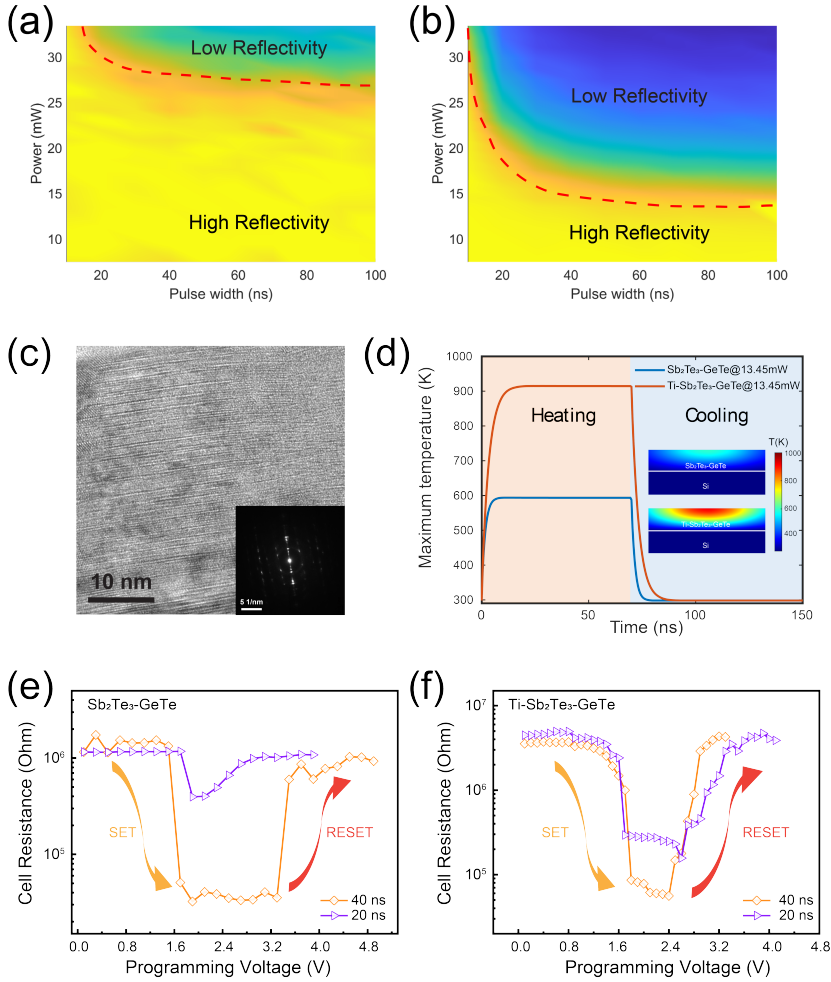


Fig. 4 Laser RESET power-time-reflectivity measurement of (a) $\text{Sb}_2\text{Te}_3\text{-GeTe}$ and (b) Ti-doped $\text{Sb}_2\text{Te}_3\text{-GeTe}$ superlattice films. (c) cross-sectional TEM image of the area after laser switching pulse. The inset image is the selected area electron diffraction pattern. (d) Heat transport simulation of superlattice films during laser RESET process. Maximum temperature on the surface of superlattice films after a 70 ns laser pulse with different powers. The temperature distribution was shown in the embedded color map. The reversible resistance switching of R-V characteristics of the (e) $\text{Sb}_2\text{Te}_3\text{-GeTe}$ and (f) Ti-doped $\text{Sb}_2\text{Te}_3\text{-GeTe}$ superlattice films.

laser and a relatively low-power 635 nm probe laser, which can measure the switching power and time [32]. The system can simultaneously capture the reflection of the probe laser from the sample whilst the pump laser pulses heat into the sample. The focused laser spot had a beam size of $0.6\ \mu\text{m}$ ($1/e^2$ intensity) on the sample. The electrical switching performance of the devices was measured using a homemade system with a sourcemeter (Keithley 2600) and pulse generator (Tektronix AWG5002B). The cell resistance of the devices was

recorded after each programming pulse at a constant voltage of 0.1 V in order to minimize the read disturbance in the device.

4.3 Modelling & Simulations

4.3.1 DFT Molecular Dynamic Calculations

DF/MD calculations were performed using the Vienna *abinitio* Simulation Package (VASP) [38] with projected augmented wave (PAW) pseudopotentials [39] and Perdew-Burke-Ernzerhof generalised gradient approximation (PBE-GGA) exchange-correlation functional [40]. The spin-orbit interaction was neglected and the vdW interaction correction method of Grimme was included [41]. The unit cell of Sb₂Te₃ with three quintuple blocks was used to explore the potential Ti sites when doping. The free energy and formation energy calculations were carried out at the Γ point in the Brillouin zone ($k=0$). The plane-wave cutoff energy was 300 eV. The chemical bonding was studied by crystal orbital Hamiltonian population (COHP) analysis with LOBSTER program [42].

The MD premelting study used a [Ti-Sb₂Te₃]_{4nm}-[GeTe]_{1nm} supercell ($3 \times 3 \times 1$) consisting of 9 Ti, 18 Ge, 63 Sb and 126 Te atoms, as shown in Fig. 1(a). The configuration of the Ti atoms, which substituted Sb atoms, were searched using `pymatgen` package [43]. The geometry relaxation of the supercell was carried out at 0 K after which NVT canonical ensemble was used to update the atomic positions every 3 fs whilst the relaxed structure was heated at 2 K/ps from 450 K to 1200 K, which is above the structure's melting point, as seen in Fig. 3. The initial velocities at 450 K were random, and scaled according to the temperature. The temperature of the model during the temperature ramp was controlled by velocity rescaling. The energy of the ensemble was computed at the Γ point in the Brillouin zone ($k=0$). The plane-wave cut-off energy for the the molecular dynamics simulations was 240 eV.

The GeTe premelting behaviour was studied by calculating the Bond Orientation Parameter (BOP) of the Ti-Sb₂Te₃ and GeTe sections of the simulation supercell, which is commonly used to identify the different local atomic crystal structures and to study structural phase transitions [31, 44]. The local structure around atom i is defined by a set of spherical harmonics, where $Y_{lm}(\hat{\mathbf{r}}_{ij})$, $\hat{\mathbf{r}}_{ij}$ is the vector between atom i and one of its neighbours j . N_b is the total number of neighbours around the i^{th} atom. The global bond order parameter, Q_l , can be then calculated by averaging according to:

$$Q_l \equiv \sqrt{\frac{4\pi}{2l+1} \sum_{m=-l}^l \left| \frac{1}{N_b} \sum_{j=1}^{N(i)} Y_{lm}(\hat{\mathbf{r}}_{ij}) \right|^2} \quad (3)$$

where $l = 4$ for a local atomic cubic structure. The layer crystallinity was calculated as an average over all the atoms occupying the space initially occupied by each layer, and over 1 ps (2 K) windows.

4.3.2 Laser-heat-induced superlattice switching simulations

Heat generated by laser pulses in the superlattice was used to induce interfacial phase transitions, see Fig. 4. We modelled the transient heating effect using a finite-difference time-domain approach to solve the unsteady heat conduction equation, as expressed in Eq. 4,

$$\rho c_p \frac{\partial T(x, y, z, t)}{\partial t} = \nabla \cdot \kappa \nabla T(x, y, z, t) + Q(x, y, z, t) \quad (4)$$

where, ρ is the mass density, c is the specific heat capacity, $T(x, y, z, t)$ is the temperature of a position of (x, y, z) at a certain moment t , κ is the thermal conductivity, $Q(x, y, z, t)$ is the Joule heat brought by the laser pulse with a Gaussian beam profile, which can be given as Eq. 5,

$$Q(x, y, z, t) = e^{-\alpha z} \frac{2P_{in}}{\pi w^2} (1 - R) \alpha e^{-2\frac{x^2+y^2}{w^2}} f(t) \quad (5)$$

where, P_{in} is the laser power, w is the $1/e^2$ Gaussian beam radius, α is the absorption coefficient, R is the reflectivity, and $f(t)$ is the temporal waveform. Here, the heat capacity (ρc_p) of $\text{Ge}_2\text{Sb}_2\text{Te}_5$ ($\sim 1.25 \times 10^6 \text{ J}\cdot\text{m}^{-3}\cdot\text{K}^{-1}$) was used [45]. α of Sb_2Te_3 – GeTe ($\sim 8.155 \times 10^7 \text{ m}^{-1}$) and Ti-doped Sb_2Te_3 – GeTe ($\sim 5.676 \times 10^7 \text{ m}^{-1}$) were calculated from measured extinction coefficient (Fig. S8). R of Sb_2Te_3 – GeTe (0.63) and Ti-doped Sb_2Te_3 – GeTe (0.50) superlattices were measured with a 660-nm laser, which are consistent with the simulated reflection from measured refractive index and extinction coefficient, as shown in Fig. S8. We measured κ of Sb_2Te_3 – GeTe ($\sim 0.49 \text{ W}\cdot\text{m}^{-1}\cdot\text{K}^{-1}$) and Ti-doped Sb_2Te_3 – GeTe ($\sim 0.24 \text{ W}\cdot\text{m}^{-1}\cdot\text{K}^{-1}$) using TDTR system (Fig. 2(a)). A 70ns laser pulse was used to simulate the temperature of the film as a function of time for different incident laser powers.

Supplementary Information. Whilst writing this article we became aware of a similar set of results from the group of Mann-ho Cho at Yonsei University, Korea. See REF XXX. The fact that two different research groups independently show similar increases in material switching efficiency and stability using different techniques lends further credibility to the results presented herein.

This article has an accompanying supplement.

Acknowledgments. The SUTD-based research was funded by two different grants: (1) Singapore Ministry of Education (MoE) award # 2017-T2-1-161, and (2) Office of Naval Research Global award # N62909-19-1-2005. Ms Jing Ning is grateful for her MoE PhD scholarship.

References

- [1] S.R. Department. Total data volume worldwide 2010-2025 (2022). URL <https://www.statista.com/statistics/871513/worldwide-data-created/>
- [2] M. Koot, F. Wijnhoven, Usage impact on data center electricity needs: A system dynamic forecasting model. *Appl. Energy* **291**, 116,798 (2021)
- [3] Y. Chen, Reram: History, status, and future. *IEEE Transactions on Electron Devices* **67**(4), 1420–1433 (2020)
- [4] S.J. Kim, J. Mohan, S.R. Summerfelt, J. Kim, Ferroelectric hf 0.5 zr 0.5 o 2 thin films: A review of recent advances. *Jom* **71**(1), 246–255 (2019)
- [5] P.K. Amiri, J.G. Alzate, X.Q. Cai, F. Ebrahimi, Q. Hu, K. Wong, C. Grèzes, H. Lee, G. Yu, X. Li, et al., Electric-field-controlled magnetoelectric ram: progress, challenges, and scaling. *IEEE Transactions on Magnetics* **51**(11), 1–7 (2015)
- [6] W. Zhang, R. Mazzarello, M. Wuttig, E. Ma, Designing crystallization in phase-change materials for universal memory and neuro-inspired computing. *Nature Reviews Materials* **4**(3), 150–168 (2019)
- [7] T. Ohta, Phase-change optical memory promotes the DVD optical disk. *Journal of Optoelectronics and Advanced Materials* **3**(3), 609–626 (2001)
- [8] J. Hruska. Intel, Micron reveal Xpoint, a new memory architecture that could outclass DDR4 and NAND (2015). URL <https://www.extremetech.com/extreme/211087-intel-micron-reveal-xpoint-a-new-memory-architecture-that-claims-to-outclass-both-ddr4-and-nand>
- [9] L. Zhang, S. Cosemans, D.J. Wouters, G. Groeseneken, M. Jurczak, B. Govoreanu, One-selector one-resistor cross-point array with threshold switching selector. *IEEE Transactions on Electron Devices* **62**(10), 3250–3257 (2015). <https://doi.org/10.1109/TED.2015.2461656>
- [10] M. Zhu, K. Ren, Z. Song, Ovonic threshold switching selectors for three-dimensional stackable phase-change memory. *MRS Bulletin* **44**(9), 715–720 (2019)
- [11] S.M. Sadeghipour, L. Pileggi, M. Asheghi, in *Thermal and Thermo-mechanical Proceedings 10th Intersociety Conference on Phenomena in Electronics Systems, 2006. IThERM 2006*. (IEEE, 2006), pp. 660–665
- [12] X. Zhou, M. Xia, F. Rao, L. Wu, X. Li, Z. Song, S. Feng, H. Sun, Understanding phase-change behaviors of carbon-doped Ge₂Sb₂Te₅ for phase-change memory application. *ACS Applied Materials & Interfaces*

6(16), 14,207–14,214 (2014)

- [13] Q. Wang, B. Liu, Y. Xia, Y. Zheng, R. Huo, Q. Zhang, S. Song, Y. Cheng, Z. Song, S. Feng, Cr-doped Ge₂Sb₂Te₅ for ultra-long data retention phase change memory. *Applied Physics Letters* **107**(22), 222,101 (2015)
- [14] Y. Wang, Y. Zheng, G. Liu, T. Li, T. Guo, Y. Cheng, S. Lv, S. Song, K. Ren, Z. Song, Scandium doped Ge₂Sb₂Te₅ for high-speed and low-power-consumption phase change memory. *Applied Physics Letters* **112**(13), 133,104 (2018)
- [15] M. Zhu, L. Wu, F. Rao, Z. Song, K. Ren, X. Ji, S. Song, D. Yao, S. Feng, Uniform ti-doped sb2te3 materials for high-speed phase change memory applications. *Appl. Phys. Lett.* **104**(5), 053,119 (2014)
- [16] T. Chong, L. Shi, R. Zhao, P. Tan, J. Li, H. Lee, X. Miao, A. Du, C. Tung, Phase change random access memory cell with superlattice-like structure. *Appl. Phys. Lett.* **88**(12), 122,114 (2006)
- [17] C.Y. Ahn, S.W. Fong, Y. Kim, S. Lee, A. Sood, C.M. Neumann, M. Ashegh, K.E. Goodson, E. Pop, H.S.P. Wong, Energy-efficient phase-change memory with graphene as a thermal barrier. *Nano Letters* **15**(10), 6809–6814 (2015). URL [⟨GotoISI⟩://WOS:000363003100079https://pubs.acs.org/doi/pdf/10.1021/acs.nanolett.5b02661](https://pubs.acs.org/doi/pdf/10.1021/acs.nanolett.5b02661)
- [18] C.M. Neumann, K.L. Okabe, E. Yalon, R.W. Grady, H.S.P. Wong, E. Pop, Engineering thermal and electrical interface properties of phase change memory with monolayer mos2. *Applied Physics Letters* **114**(8) (2019). URL [⟨GotoISI⟩://WOS:000460134000016](https://pubs.acs.org/doi/pdf/10.1021/acs.nanolett.5b02661)
- [19] J. Ning, Y. Wang, T.Y. Teo, C.C. Huang, I. Zeimpekis, K. Morgan, S.L. Teo, D.W. Hewak, M. Bosman, R.E. Simpson, Low energy switching of phase change materials using a 2d thermal boundary layer. *ACS Applied Materials & Interfaces* **14**(36), 41,225–41,234 (2022). <https://doi.org/10.1021/acsami.2c12936>. URL <https://doi.org/10.1021/acsami.2c12936>
- [20] R. Simpson, P. Fons, A. Kolobov, T. Fukaya, M. Krbal, T. Yagi, J. Tom-inaga, Interfacial phase-change memory. *Nat. Nanotechnol.* **6**(8), 501 (2011)
- [21] H. Kwon, A.I. Khan, C. Perez, M. Asheghi, E. Pop, K.E. Goodson, Uncovering thermal and electrical properties of sb2te3/gete superlattice films. *Nano Letters* **21**(14), 5984–5990 (2021). <https://doi.org/10.1021/acs.nanolett.1c00947>. URL <https://doi.org/10.1021/acs.nanolett.1c00947>. PMID: 34270270. <https://arxiv.org/abs/https://doi.org/10.1021/acs.nanolett.1c00947>

- [22] J. Kalikka, X. Zhou, E. Dilcher, S. Wall, J. Li, R.E. Simpson, Strain-engineered diffusive atomic switching in two-dimensional crystals. *Nature communications* **7**(1), 1–8 (2016)
- [23] X. Zhou, J.K. Behera, S. Lv, L. Wu, Z. Song, R.E. Simpson, Avalanche atomic switching in strain engineered sb₂te₃–gete interfacial phase-change memory cells. *Nano Futures* **1**(2), 025,003 (2017)
- [24] Č. Drašar, M. Steinhart, P. Lošt'ák, H.K. Shin, J. Dyck, C. Uher, Transport coefficients of titanium-doped sb₂te₃ single crystals. *Journal of Solid State Chemistry* **178**(4), 1301–1307 (2005)
- [25] J. Tominaga, S. Sumi, H. Awano, Intermixing suppression through the interface in gete/sb₂te₃ superlattice. *Applied Physics Express* **13**(7), 075,503 (2020)
- [26] A.I. Khan, X. Wu, C. Perez, B. Won, K. Kim, P. Ramesh, H. Kwon, M.C. Tung, Z. Lee, I.K. Oh, K. Saraswat, M. Asheghi, K.E. Goodson, H.S.P. Wong, E. Pop, Unveiling the effect of superlattice interfaces and intermixing on phase change memory performance. *Nano Letters* **22**(15), 6285–6291 (2022). <https://doi.org/10.1021/acs.nanolett.2c01869>. URL <https://doi.org/10.1021/acs.nanolett.2c01869>. PMID: 35876819. <https://arxiv.org/abs/https://doi.org/10.1021/acs.nanolett.2c01869>
- [27] D.M. Rowe, *CRC handbook of thermoelectrics* (CRC press, 2018)
- [28] J.L. Lensch-Falk, D. Banga, P. Hopkins, D. Robinson, V. Stavila, P. Sharma, D. Medlin, Electrodeposition and characterization of nano-crystalline antimony telluride thin films. *Thin Solid Films* **520**(19), 6109–6117 (2012)
- [29] S. Shen, W. Zhu, Y. Deng, H. Zhao, Y. Peng, C. Wang, Enhancing thermoelectric properties of sb₂te₃ flexible thin film through microstructure control and crystal preferential orientation engineering. *Applied Surface Science* **414**, 197–204 (2017)
- [30] X. Zhou, J. Kalikka, X. Ji, L. Wu, Z. Song, R.E. Simpson, Phase-change memory materials by design: a strain engineering approach. *Advanced Materials* **28**(15), 3007–3016 (2016)
- [31] P.J. Steinhart, D.R. Nelson, M. Ronchetti, Bond-orientational order in liquids and glasses. *Phys. Rev. B* **28**(2), 784 (1983)
- [32] J.K. Behera, X. Zhou, J. Tominaga, R.E. Simpson, Laser switching and characterisation of chalcogenides: systems, measurements, and applicability to photonics. *Optical Materials Express* **7**(10), 3741–3759 (2017)

- [33] S.R. Ovshinsky, Reversible electrical switching phenomena in disordered structures. *Physical Review Letters* **21**(20), 1450 (1968)
- [34] Y. Saito, P. Fons, L. Bolotov, N. Miyata, A.V. Kolobov, J. Tomimaga, A two-step process for growth of highly oriented sb2te3 using sputtering. *Aip Advances* **6**(4), 045,220–045,220 (2016). <https://doi.org/Artn04522010.1063/1.4948536>. URL [⟨GotoISI⟩://WOS:000375845100066https://aip.scitation.org/doi/pdf/10.1063/1.4948536](https://doi.org/10.1063/1.4948536)
- [35] J. Ning, J.C. Martinez, J. Momand, H. Zhang, S.C. Tiwari, F. Shimojo, A. Nakano, R.K. Kalia, P. Vashishta, P.S. Branicio, B.J. Kooi, R.E. Simpson, Differences in sb2te3 growth by pulsed laser and sputter deposition. *Acta Materialia* **200**, 811–820 (2020). <https://doi.org/10.1016/j.actamat.2020.09.035>. URL [⟨GotoISI⟩://WOS:000580631600068](https://doi.org/10.1016/j.actamat.2020.09.035)
- [36] Y. Yamashita, Y. Aoki, T. Yagi, J. Jia, M. Kashiwagi, Y. Oguchi, N. Take-toshi, Y. Shigesato, Thermal conductivity across the van der waals layers of α -MoO₃ thin films composed of mosaic domains with in-plane 90° rotations. *Journal of Applied Physics* **130**(8), 085,103 (2021)
- [37] Y. Isosaki, Y. Yamashita, T. Yagi, J. Jia, N. Taketoshi, S. Nakamura, Y. Shigesato, Structure and thermophysical properties of GaN films deposited by reactive sputtering using a metal Ga target. *Journal of Vacuum Science & Technology A: Vacuum, Surfaces, and Films* **35**(4), 041,507 (2017)
- [38] G. Kresse, J. Hafner, Ab initio molecular dynamics for liquid metals. *Phys. Rev. B* **47**(1), 558–561 (1993)
- [39] G. Kresse, D. Joubert, From ultrasoft pseudopotentials to the projector augmented-wave method. *Phys. Rev. B* **59**(3), 1758–1775 (1999)
- [40] J.P. Perdew, K. Burke, M. Ernzerhof, Generalized gradient approximation made simple. *Phys. Rev. Lett.* **77**(18), 3865–3868 (1996)
- [41] S. Grimme, J. Antony, S. Ehrlich, H. Krieg, A consistent and accurate ab initio parametrization of density functional dispersion correction (dft-d) for the 94 elements h-pu. *The Journal of chemical physics* **132**(15), 154,104 (2010)
- [42] R. Dronskowski, P.E. Bloechl, Crystal orbital Hamilton populations (COHP): energy-resolved visualization of chemical bonding in solids based on density-functional calculations. *The Journal of Physical Chemistry* **97**(33), 8617–8624 (1993)
- [43] S.P. Ong, W.D. Richards, A. Jain, G. Hautier, M. Kocher, S. Cholia, D. Gunter, V.L. Chevrier, K.A. Persson, G. Ceder, Python materials

genomics (pymatgen): A robust, open-source python library for materials analysis. *Computational Materials Science* **68**, 314–319 (2013)

- [44] J. Kalikka, J. Akola, J. Larrucea, R. Jones, Nucleus-driven crystallization of amorphous ge 2 sb 2 te 5: A density functional study. *Phys. Rev. B* **86**(14), 144,113 (2012)
- [45] J. Reifenberg, E. Pop, A. Gibby, S. Wong, K. Goodson, in *Thermal and Thermomechanical Proceedings 10th Intersociety Conference on Phenomena in Electronics Systems, 2006. I THERM 2006*. (IEEE, 2006), pp. 106–113

5 Supplementary Information

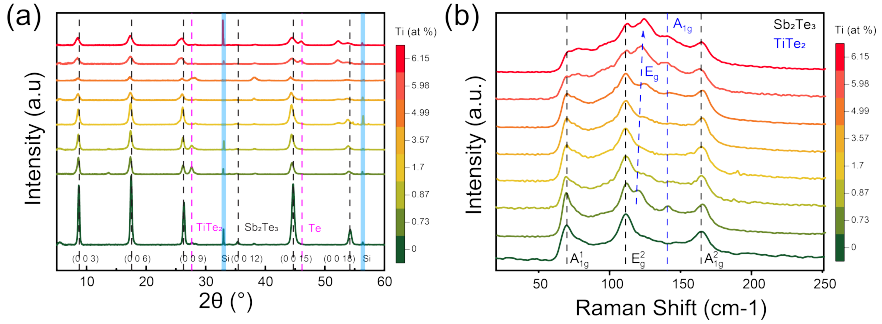


Fig. S1 (a) XRD patterns and (b) Raman spectra of pure Sb_2Te_3 and doped Sb_2Te_3 films with different concentration of Ti. The concentration of Ti was shown in the color range from green to red.

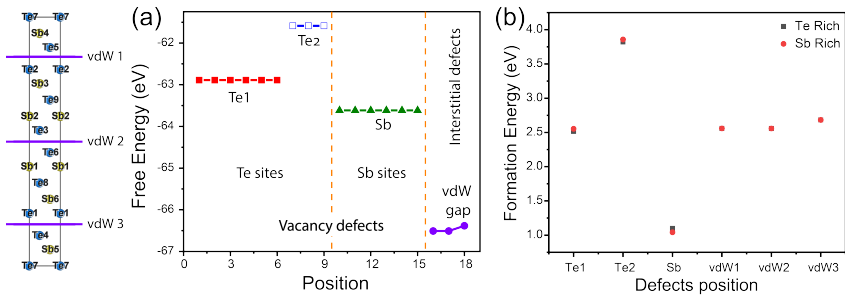


Fig. S2 (a) Free energy and (b) Formation energy calculation of structures with different Ti defects. Defects sites were labelled in the Sb_2Te_3 structure.

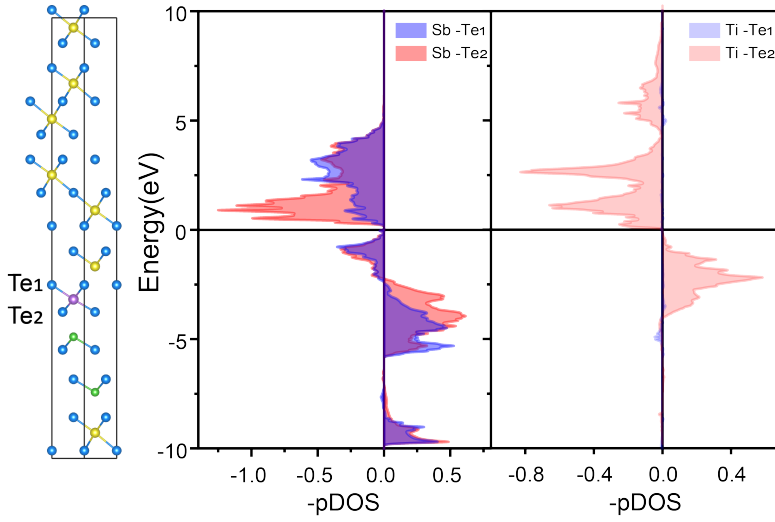


Fig. S3 Bonding states comparison of Sb or Ti and its neighbors in superlattice structure.

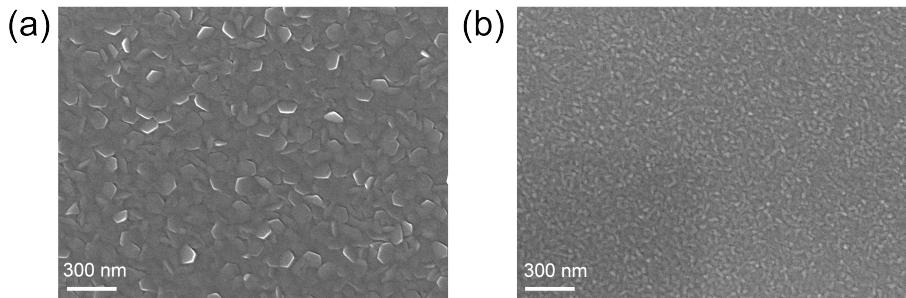


Fig. S4 Morphology of (a) $\text{Sb}_2\text{Te}_3\text{-GeTe}$ and (b) Ti-doped $\text{Sb}_2\text{Te}_3\text{-GeTe}$ superlattice films.

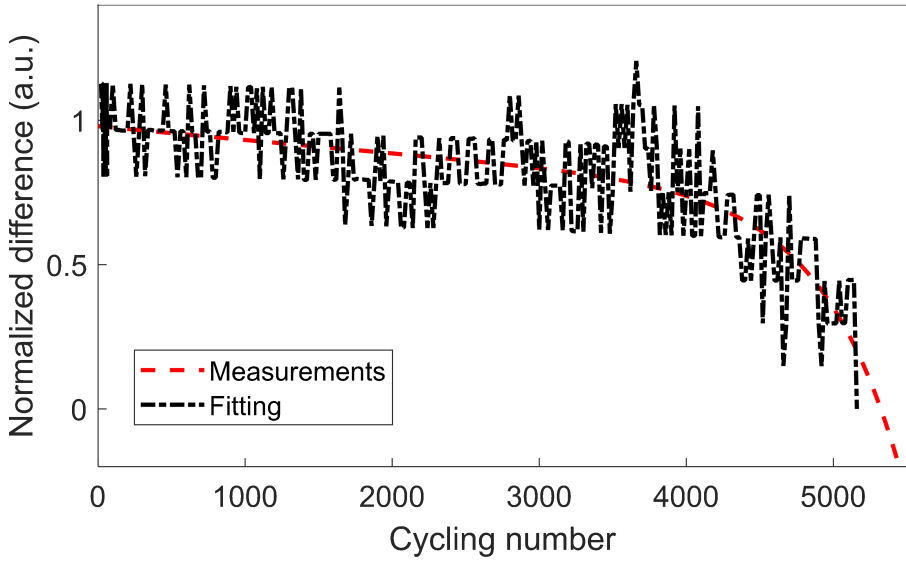


Fig. S5 The endurance-cycling measurements for the Ti-doped Sb_2Te_3 -GeTe superlattice structure using 50ns, 13.45 mW and 300 ns, 9.42 mW as RESET and SET pulses, respectively.

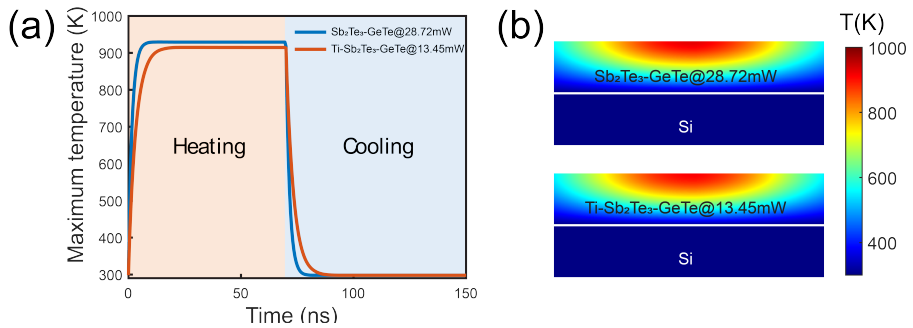


Fig. S6 Heat transfer simulation of Sb_2Te_3 -GeTe and Ti-doped Sb_2Te_3 -GeTe in RESET operation.

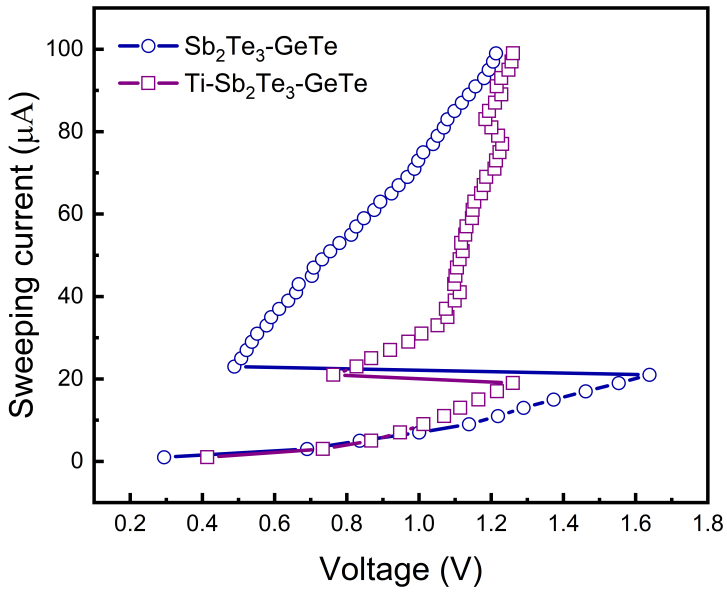


Fig. S7 The threshold switching characteristics of the undoped and Ti-doped $\text{Sb}_2\text{Te}_3\text{-GeTe}$ superlattice iPCM devices.

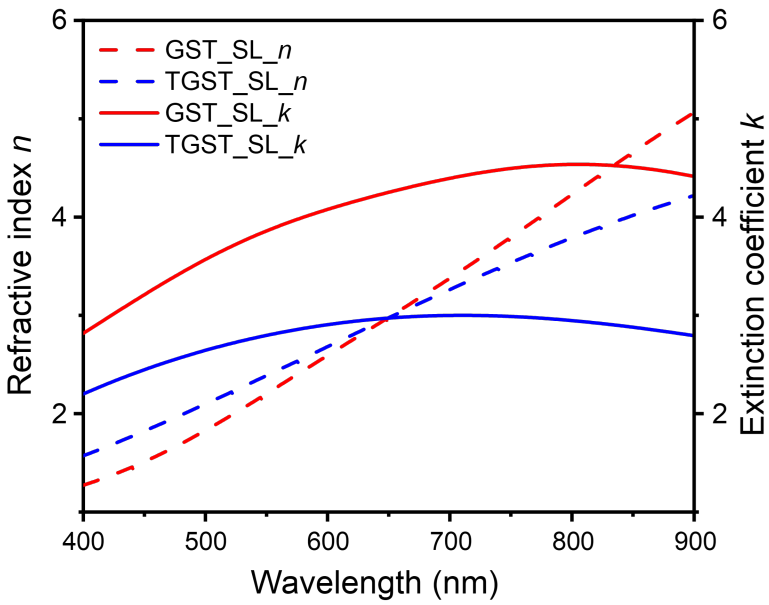


Fig. S8 Optical properties of two superlattice films. Refractive index, n , and extinction coefficient is displayed as dash-line and line, respectively.